Available on CMS information server

CMS NOTE 1997/078

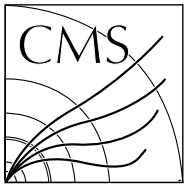

The Compact Muon Solenoid Experiment

CMS Note

Mailing address: CMS CERN, CH-1211 GENEVA 23, Switzerland

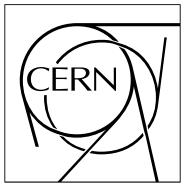

9 July 1997

Tests of Cathode Strip Chamber Prototypes

M.M. Baarmand[7)], Yu. Bonushkin[1)], D. Chrisman[2)], S. Durkin[9)], T. Ferguson[3)], P. Giacomelli[2)], L. Gorn[4)], W. Gorn[2)], J. Hauser[1)], J. Hirschfelder[3)], J. Hoftiezer[9)], H. Hoorani[3)], O. Kisselev[10)], D.E. Klem[6)], A. Korytov[4)], J.G. Layter[2)], P. Lennous[9)], T.Y. Ling[9)], C. Matthey[1)], S. Medved[11)], C. Minor[2)], G. Mitselmakher[4)], T. Muller[1,a)], S. Otwinowski[1)], L. Preston[11)], O. Prokofiev[10)], C. Rush[9)], P. Schenk[2,b)], Y. Sedykh[5)], I. Smirnov[10)], V. Soulimov[10)], A. Vaniachine[7,c)], T. Vercelli[6)], E. von Goeler[8)], C. Wuest[6)], J. Zeng[1)].

Abstract

We report on the results of testing two six-layer $0.6 \times 0.6\ \mathrm{m}^2$ cathode strip chamber (CSC) prototypes in a muon beam at CERN. The prototypes were designed to simulate sections of the end-cap muon system of the Compact Muon Solenoid (CMS) detector which will be installed at the Large Hadron Collider (LHC). We measured the spatial and time resolutions of each chamber for different gains, different orientations with respect to the beam direction and different strength magnetic fields. The single-layer spatial resolution of a prototype with a strip pitch of 15.88 mm ranged from 78 μm to 468 μm, depending on whether the particle passed between two cathode strips or through the center of a strip; its six-layer resolution was found to be 44 μm. The single-layer spatial resolution of a

[1)] University of California Los Angeles

[2)] University of California Riverside

[3)] Carnegie Mellon University

[4)] University of Florida

[5)] Joint Institute for Nuclear Research, Dubna

[6)] Lawrence Livermore National Laboratory

[7)] State University of New York Stony Brook

[8)] Northeastern University

[9)] Ohio State University

[10)] Petersburg Nuclear Physics Institute

[11)] Purdue University

[a)] Now at Institut für Experimentelle Kernphysik, Karlsruhe, Germany.

[b)] Now at Andersen Consulting, Fredericton, New Brunswick, Canada.

[c)] Now at Royal Institute of Technology, Stockholm, Sweden.

prototype with a strip pitch of 6.35 mm ranged from 54 μm to 66 μm; its six-layer resolution was found to be 23 μm. The efficiency for collecting an anode wire signal from one of six layers within a 20 ns time window appropriate for the LHC was found to be greater than 95% in normal running conditions.

To be published in *Nuclear Instruments and Methods*

1 Introduction

This paper describes the results from testing two Cathode Strip Chamber (CSC) prototypes in a muon beam at CERN. The prototypes were designed to represent small sections of the ultimately large CSCs to be built for the end-cap muon system of the CMS Detector [1]. The CMS end-cap muon system will have 540 6-layer CSCs, almost half of them being 3.4×1.5 m^2 in size. The required spatial resolution, combining all six layers of the chamber, is limited by multiple scattering, and ranges from 75 μm for smaller chambers (closer to the interaction point) to 150 μm for the larger chambers. Each chamber should tag the bunch crossing associated with registered tracks with high efficiency in order to use them in the first-level trigger. (Bunch crossings at LHC will be separated by 25 ns.) Expected charged particle background rates can be as high as 100-1000 Hz/cm^2. In addition, some of the chambers will have to operate in a high ($\sim$4 T) and often non-uniform magnetic field.

Cathode Strip Chamber technology [2] is a natural choice for the conditions and requirements outlined above. A CSC is a multi-wire proportional chamber with a cathode segmented in strips. The precision measurement of a track coordinate is based on finding the center of the charge distribution induced on the strips. The CMS CSCs will be trapezoidal with cathode strips running radially, providing a precise measurement of the azimuthal coordinate. Anode wires will be grouped with a segmentation ranging from 2 to 5 cm, to provide an approximate radial coordinate measurement and the precise timing information for tagging the beam-crossing. Chambers at the inner radius will cover 20 degrees in azimuthal angle, while those at the outer radius will be divided in 10 degree sectors.

2 CSC Prototypes

The two prototypes (P0 and P0$'$) were built using 12.5 mm thick aluminum honeycomb panels with skins made of copper-clad FR4[1)] sheets. Seven such panels were stacked together to form a 6-gap chamber (see Fig. 1). Each full gas gap (cathode-to-cathode) is $2h$ = 9.53 mm, where h is the distance between the cathode plane and the anode wires. The P0 prototype had 32 strips per layer, with a strip pitch of 15.88 mm, which is the strip pitch at the outer radius of the largest CMS chambers. The strips were separated by a 1 mm gap. A constant strip pitch of 15.88 mm is unusually large for a chamber with a full gas gap of 9.53 mm. The optimal strip pitch for this gas gap is about 6 mm [3]; this latter value was implemented in the P0$'$ chamber, which represents the innermost part of the smaller CMS CSCs. In both prototypes, the strips were oriented perpendicular to the wires. Because the 3.2 mm thick FR4 skins had copper on both sides, the strip-to-ground capacitance was large (240 pF for P0 and 160 pF for P0$'$). This allowed us to simulate the large strip capacitance and realistic noise of the CMS chambers whose FR4 skins will be clad with copper on one side only, but whose strips will be as long as 3.3 m.

The P0 prototype had 30 μm diameter wires spaced by 2.5 mm, while the P0$'$ prototype had 50 μm wires 3.4 mm apart. These two combinations resulted in about the same operational high voltages, around 4 kV. The second combination is more attractive from the chamber construction point of view: the wires are much stronger and will not require intermediate supports over the maximum 1.3 m span in the largest CMS chambers. The only concern was whether the time resolution of the chamber with the larger wire spacing would be sufficient. The wires were interconnected to form 3 cm wide anode wire groups. The P0 prototype had 192 anode wires per layer, grouped in 12 wires per readout channel. The P0$'$ prototype had 144 wires per layer, grouped in 9 wires per readout channel. The design parameters of P0 and P0$'$ are summarized in Table 1.

The cathode readout electronics were based on the GASPLEX chip [4]. This front-end ASIC contains 16 charge-sensitive amplifier/shaper channels. The full range of the amplifier is about 200 fC and the equivalent input noise was measured to be 0.8 fC for P0 and 0.6 fC for P0$'$. The charge induced on each strip was integrated with a shaping time of 500 ns. Two custom-made CAMAC modules with 10-bit ADCs were used for the sequential readout of the resulting voltages.

The anode electronics employed a discrete bipolar front-end and an ECL discriminator and back-end. The front-end amplifiers implemented a 5-pole, 1-zero response and achieved an equivalent input noise at 240 pF of about 1.1 fC (7000 e$^-$). The output pulse from these amplifiers is bipolar and has a peaking time of 30 ns. The 600 MHz ECL comparator scheme used to discriminate the pulse provided either leading-edge (threshold) or zero-crossing timing information, selectable by a jumper. The threshold level was remotely adjustable and typically set to about 7 fC[2)]. For the P0$'$ data one half of the chamber was configured for zero-crossing and the other half configured for

[1)] FR4 is a non-flammable fiberglass reinforced epoxy.

[2)] The anode current was twice that of one of the two cathodes, but given the large difference in the shaping times of the anode and cathode electronics which produces almost a factor of 3 difference in integrated charge, this anode threshold was

	P0	P0′
Full gas gap ($2h$) [mm]	9.53	9.53
Wire diameter [μm]	30	50
Wire spacing [mm]	2.5	3.4
Number of wires per anode channel	12	9
Cathode strip pitch [mm]	15.88	6.35
Cathode strip separation [mm]	1.0	1.0
Chamber instrumented area [cm^2]	50×50	20×50
Number of layers	6	6
Anode channels per layer	16	16
Cathode channels per layer	32	32

Table 1: Design parameters of the P0 and P0′ prototypes.

leading-edge. For the P0 data the entire chamber was configured for leading-edge.

The ECL levels produced by the discriminators were converted to differential ECL and used to drive twisted-pair cables to the remotely located counting house, where they were digitized using LeCroy 2277 multi-hit TDCs with 1 ns resolution.

It is worth pointing out that the final electronics being designed for the CSC chambers will be different from what were used in our tests. For instance, the cathode electronics will have a 100 ns peaking time, an equivalent noise of 1 fC and a full dynamic range of 2 pC. Analog information will be stored in switched capacitor arrays and then multiplexed for digitization by 12-bit ADCs. The anode electronics will have about the same 30 ns shaping time as the electronics used in our tests, but will have constant-fraction discriminators.

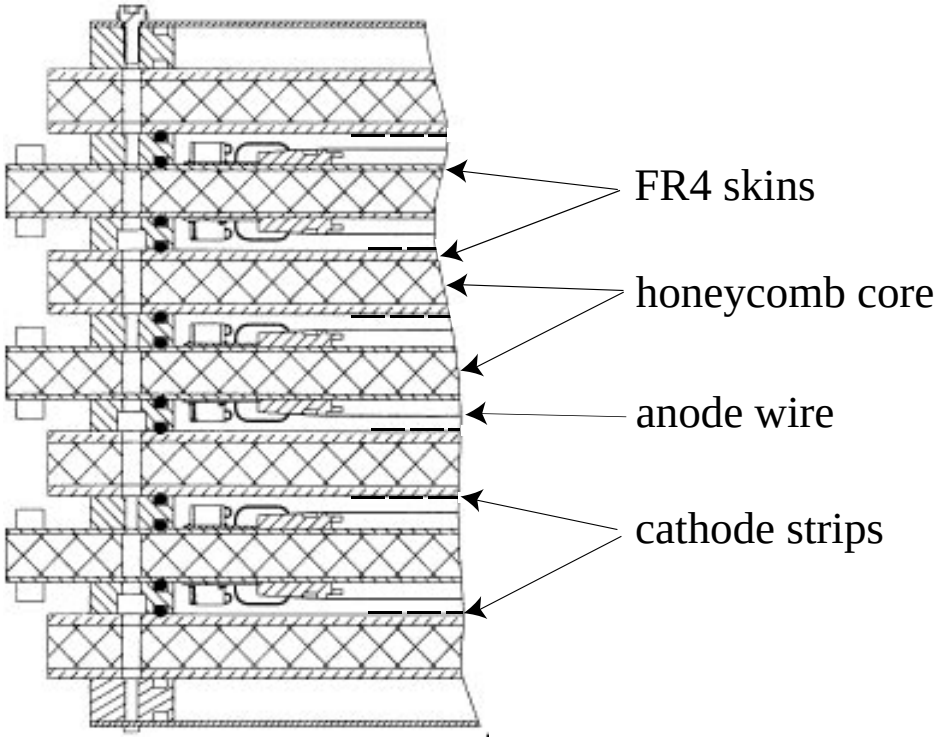

Figure 1: Cross-section of the 6-layer CSC prototype P0′.

approximately equivalent to a charge of $\frac{3}{2} \times 7$ fC ≈ 11 fC on the cathodes. A more accurate relationship between anode and cathode thresholds can be deduced from Fig. 3.

3 Experimental Conditions

The tests were performed using the CMS test-beam facility at the H2 beam line of the CERN SPS accelerator. Data were taken with muon beams of momenta 150, 225 and 300 GeV/c.

The experimental coordinate system is shown in Fig. 2. The z-axis is the nominal beam direction and is defined to be normal to the plane formed by the cathode strips and anode wires. The x-axis points along the anode wires, the y-axis along the cathode strips. In this coordinate system, the x position of a particle passing through a layer of the chamber is determined by finding the center of the charge distribution induced on the strips, while the y coordinate is determined by which anode wire group is hit. Figure 2 also shows the angle θ which is varied by rotating the chamber about the x-axis, and the angle ϕ which is varied by rotating the chamber about the y-axis.

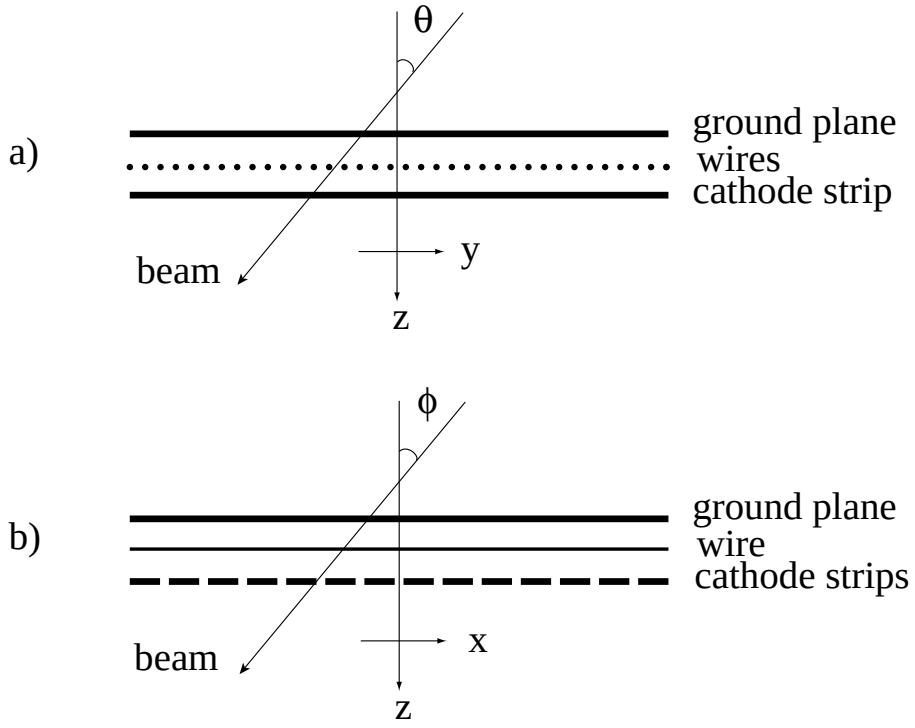

Figure 2: Schematic of the chamber coordinate system showing a) the wire angle, θ, and b) the strip angle, ϕ. During data taking, one of the angles was set to zero while the other was varied by rotating the chamber with respect to the beam. The figure is drawn approximately to scale for P0′.

For the tests conducted during the summer of 1995, the P0 chamber was located inside a magnet. Data were taken at magnetic fields ranging from 0 to 3 T. The magnetic field was parallel to the beam line. No magnetic field was used in the summer 1996 tests of the P0′ chamber. In both cases, the chamber was mounted on a platform which could rotate about the vertical axis.

The nominal gas mixture used for testing P0 was 30% Ar + 50% CO_2 + 20% CF_4, while for P0′ the gas mixture was 30% Ar + 40% CO_2 + 30% CF_4.

The H2 trigger system consisted of several scintillators upstream of the chamber. A coincidence between two of these counters was used as a trigger to define the arrival time of a muon. The overlapping area of these two counters was $10 \times 10\ \mathrm{cm}^2$. A third counter ($2 \times 2\ \mathrm{cm}^2$) was sometimes used to further restrict the beam position.

A Silicon Beam Telescope (SiBT) [5], located five meters upstream of P0′, was used to obtain a precise measurement of the incident muon's trajectory during the summer 1996 tests. The telescope is an eight-plane silicon micro-strip detector with each plane covering an area of $2.6 \times 5.8\ \mathrm{cm}^2$ and equipped with analog readout electronics. The strips have a pitch of 50 μm and are 5.8 cm long. Four of the eight planes measure the horizontal coordinate and the other four measure the vertical one. The uncertainty in the extrapolated track position at the CSC was 100 μm in both x and y.

4 Cathode and Anode Efficiencies

The cathode strip efficiency per layer was defined as the probability to find in one layer a strip signal above a threshold of 6 fC on the strip predicted by the track trajectory, or on either of its nearest neighbors. The track trajectory was determined from the other five layers.

The anode wire efficiency was defined as the probability to find in one layer a wire hit in a 100 ns window in the wire group predicted by the track trajectory or in the nearest neighboring wire group. Since the wires don't measure position very precisely, we used the SiBT to predict the wire group. To confirm the telescope prediction, we looked at the other five anode layers, requiring at least one wire hit on the track trajectory in the first three layers, at least one in the last three layers and no more than two wire hits in any one layer.

These single-layer efficiencies are shown for P0′ in Fig. 3 for events with confirmed tracks in both projections, as a function of the peak of a Landau function fitted to the distribution of the cluster charge measured with the cathode strips (see Section 5.2). The wire efficiencies shown are for threshold discriminators. The combined efficiency is the probability of finding both a strip signal and a wire signal. They are very strongly correlated, except at very low voltages; if there is a wire signal there is nearly always a strip signal. One sees that both the cathode strips and anode wires are fully efficient for a Landau peak position of 100 fC or greater. Unless otherwise stated, the results presented below are from data taken with the chamber at a nominal high voltage of 4.0 kV which resulted in a Landau peak position of 100 fC.

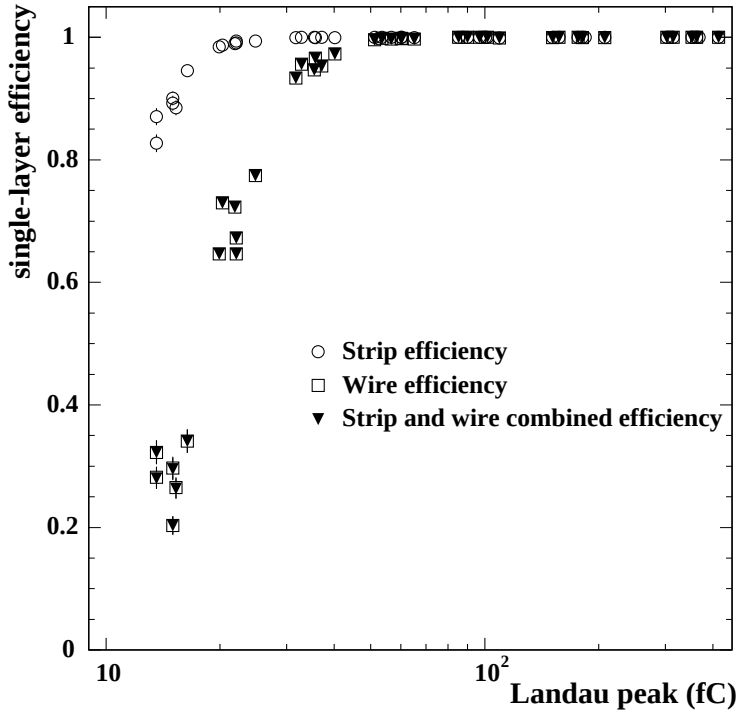

Figure 3: Single-layer efficiencies for P0′ as a function of the peak of a Landau function fitted to the distribution of the cluster charge measured with the cathode strips. The six layers are shown separately. The wire efficiencies shown are for threshold discriminators. The combined strip and wire efficiency is the fraction of tracks with both a strip cluster and a wire hit.

5 Spatial Resolution Based on Strip Charge Measurements

The track position measurement in x was obtained by finding the cathode strip cluster positions in each layer and then fitting the positions in the six layers with a straight line, after applying calibration parameters: pedestals, electronics gain, crosstalk and geometric offsets.

5.1 Calibration and Parameter Tuning

The cathode strip electronics were calibrated by measuring the responses of all strips to voltage step functions applied to each strip in turn. We used a linear fit to the response of each channel to measure the gain and the degree of crosstalk between adjacent channels, which was about 3%. The measured nonlinearity was less than 1%. Pedestals were measured at least every few hours, and in 1996 were also monitored by mixing random triggers with beam triggers. The conversion from strip channel ADC value to strip charge was derived from the calibration constants and applied to the data before any other strip analysis was done.

Three geometric parameters of the chambers are important for the position measurement: the relative offsets of the layers in the x direction, the anode-to-cathode spacing and, for inclined tracks, the layer-to-layer spacing. These parameters were determined from the data as follows.

We began by finding strip clusters. A cluster was defined as a group of five adjacent strips, the center strip of which had a charge greater than a fixed threshold and greater than the charge of either of its neighbors. The charge distribution of each cluster was fitted with a theoretical shape q(x/h), where h is the anode-to-cathode distance and x is the distance from the center of the strip with the largest charge. Cluster fitting is described in more detail in Section 5.2. The constant h was determined for each layer by finding the value which gave the minimum mean cluster-fit χ^2. The nominal cathode-to-anode spacing was 4.8 mm, and the measured values ranged from 4.7 to 5.0 mm; these values did not depend on the running conditions. Tuning h in this way significantly reduces x-dependent systematic errors in the x measurement.

The chambers were intended to have the strips in alternate layers offset by exactly one-half strip. The actual offsets were found by measuring the mean cluster offset in each layer relative to the first layer. The residuals when these mean offsets were fitted to a straight line were the measured plane misalignments, which were less than 0.4 mm. The maximum relative rotation of the strip planes about the z-axis was about 1 mrad. This is small and was not corrected for in the analysis except by readjustment of the layer offset corrections when the chamber was moved in the y-direction.

To be able to use a single set of layer offsets for different track inclination angles, we also needed a good measurement of the layer-to-layer spacing of the anode planes. This was obtained by measuring the layer offsets for four runs with different track angles, and simultaneously fitting them to four straight lines with the layer spacings, angles and offsets as free parameters. The fitted values for the layer spacings differed from the nominal spacings (approximately 26 mm) by less than 1 mm.

5.2 Single-Layer Spatial Resolution

The strip analysis begins by finding clusters in each layer, with a cluster defined as any group of five strips whose central strip charge is both a local maximum and above a fixed threshold (6 fC). The charge on the five strips was fitted to the integral of the charge distribution model derived by Gatti et al. [3]:

$$\Gamma(\lambda) = \mathrm{k}_1[(1 - \tanh^2(\mathrm{k}_2\lambda))/(1 + \mathrm{k}_3\tanh^2(\mathrm{k}_2\lambda))],$$

where Γ is the linear charge density normalized to the total anode charge and λ is the x distance from where the track crossed the wire plane divided by h, the anode-to-cathode distance. To good approximation [6], the constants k_1 and k_2 are functions only of another constant k_3, which depends on h and the anode wire radius and spacing. The Gatti distribution is shown in Fig. 4, along with the P0 and P0′ strip widths. (The strip pitches are 15.88 mm for P0 and 6.35 mm for P0′.) Due to the different wire geometry of the two prototypes, $\mathrm{k}_3 = 0.30$ for P0 and $\mathrm{k}_3 = 0.37$ for P0′, but in Fig. 4 the shape difference is imperceptible. The fit has two free parameters, x_c, the cluster peak position (the estimate of where the track crossed the strip layer), and q_c, the total charge of the cluster. No fit was done for clusters which had an ADC overflow in more than one strip. An ADC overflow occurred when the charge on a cathode strip was larger than approximately 160 fC. Two adjacent clusters whose center strips were separated by fewer than four intermediate strips were called a “double-cluster”; they were fitted with two overlapping integrated Gatti functions if neither cluster contained an ADC overflow. Overlapping clusters in groups of three or more and clusters on the edges of the chamber were not fitted. At nominal voltage, 10% of all clusters were not fitted, almost all because they contained more than one ADC overflow.

Figure 5 shows, for both P0 and P0′, the measured fraction of the total cluster charge contained on one strip, as a function of the position of that strip’s center relative to the fitted cluster position, in units of strip pitch. For example, a strip whose center is located 0.2 strip pitches away from the fitted cluster position contains on average

90% of the total cluster charge for P0, but only 63% for P0′. The error bars represent the RMS spread of the mean fraction of the total cluster charge contained on each strip. Also shown in this figure are the theoretical predictions for each strip position of P0 and P0′, which were obtained by integrating the Gatti distribution shown in Fig. 4 over the width of each strip, with the strip position located at the center of the integration range. The cluster position was obtained by fitting the charge on the strips to this function. The data agree very well with the theoretical curves; the discrepancy is smaller than 10^{-2} (in relative charge units).

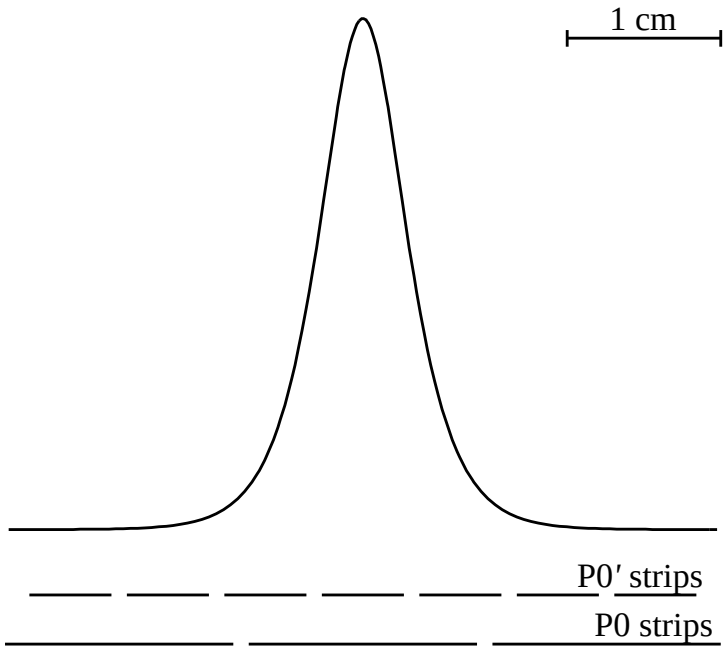

Figure 4: The theoretical Gatti charge distribution. The strip widths for P0 and P0′ are also shown.

Figure 6 displays the relation between the anode wire high voltage and the peak of a Landau function fitted to the distribution of the cluster charge measured with the strips. For these distributions the chamber was at an angle θ = 15° with respect to the beam. Also shown as an inset on this figure is a typical distribution of the cluster charge. The large error on the determination of the Landau peak at 4.2 kV in Fig. 6 occurred because a large number of clusters had multiple ADC overflows at that voltage.

To measure the single-layer spatial resolution, we selected events with only one track in the x-projection. (Rejected events which had more than one layer with more than one cluster (5%) were candidates for multiple-track events, which will be discussed in Section 5.4.) We next chose one layer, A, for study and made more cuts on the other five layers to select well-measured tracks. These layers were considered "good" if they had exactly one cluster, no ADC overflows, and the cluster had a good cluster-fit χ^2. (The cluster χ^2 cut was adjusted to keep approximately 90% of all clusters.) Tracks were found by making a straight-line fit to the cluster positions in the good layers (excluding layer A). The errors assigned to the cluster position measurements were inversely proportional to the cluster charges and, for P0, also depended on x_c, the fitted cluster position. (Clusters which were centered on a strip were less well measured.) The x_c dependence was determined from simulation. Events were rejected which had fewer than three out of five good layers (4%) or which had a bad track-fit χ^2 (8%) (the track χ^2 cut was adjusted to keep approximately 90% of all tracks). The percentages of rejected events given above were for P0′ data with the Landau peak position at 100 fC and $\theta = 15°$. No cuts were made on layer A.

The single-layer spatial resolution was defined as the standard deviation of a Gaussian fitted to the residual distribution $x_c(A) - x_t(A)$, where $x_c(A)$ is the fitted cluster position in layer A and $x_t(A)$ the interpolated track position in layer A. This distribution is shown in Fig. 7a for layer 3 of P0. Layer 3 was chosen because the error on $x_t(A)$ is smaller (35 to 53 μm for P0 and 24 μm for P0′) for the inner layers of the chamber.

We define a variable x_s, which is the distance between $x_t(A)$ and the center of the nearest strip, divided by the strip pitch. A track which passes through the center of a strip has an x_s value of zero, while a track passing between

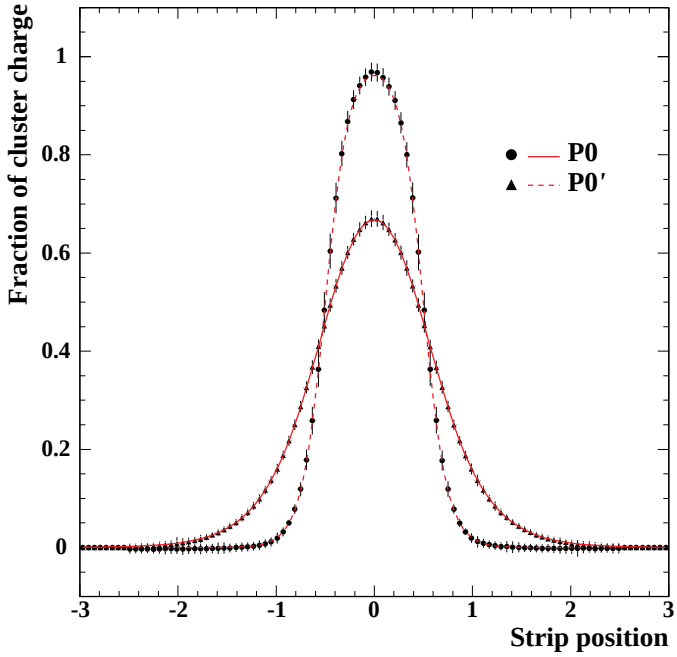

Figure 5: Fraction of the total cluster charge contained on one cathode strip as a function of the position of that strip's center relative to the fitted cluster position, in units of strip pitch. The symbols are the P0 and P0′ data; the solid curves show the prediction from the integrated Gatti function.

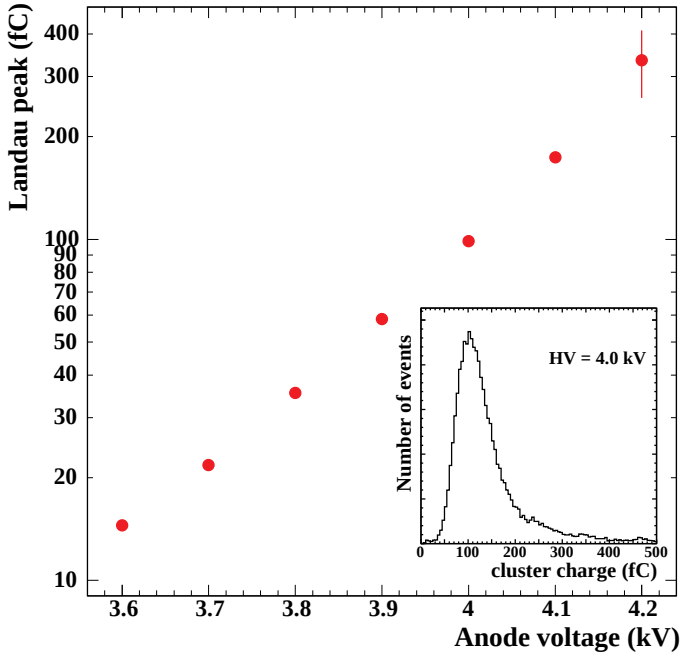

Figure 6: Peak of a Landau function fitted to the distribution of the cluster charge measured with the strips, for P0′, as a function of anode high voltage. A typical distribution of the cluster charge for data taken a 4.0 kV is also shown as an inset. The uncertainty on the point at 4.2 kV is caused by a large number of clusters with multiple ADC overflows.

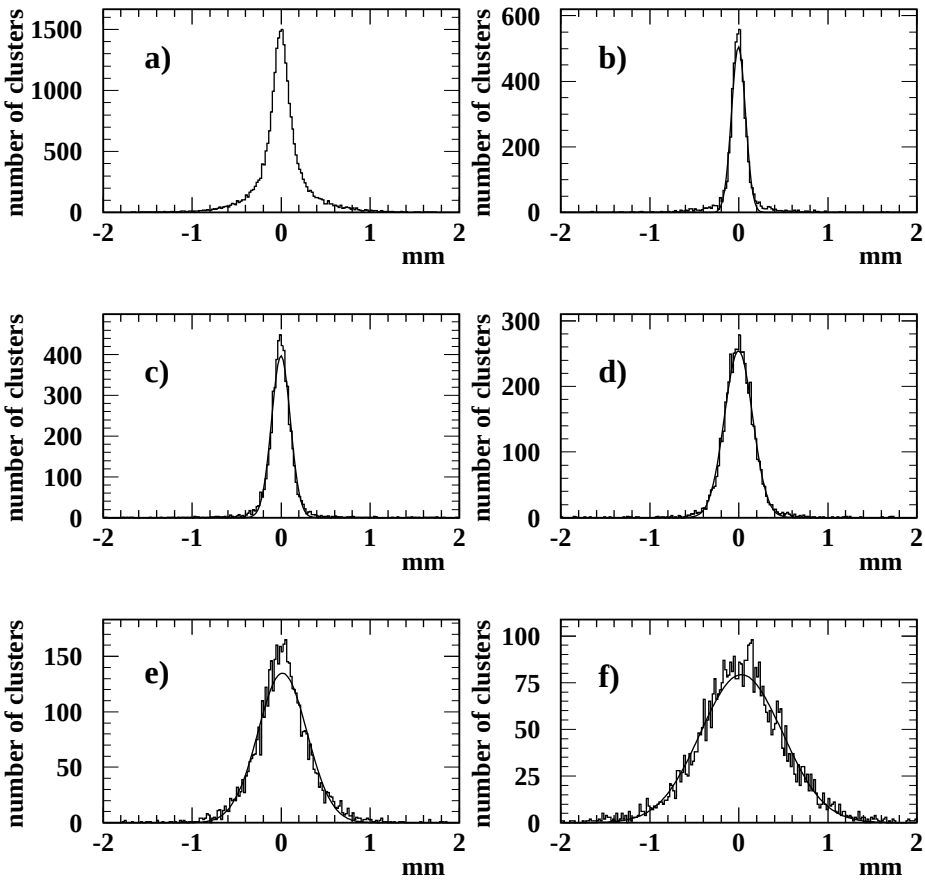

Figure 7: Single-layer residual distributions in layer 3 of P0 for a) all x_s, b) $0.4 < x_s < 0.5$, c) $0.3 < x_s < 0.4$, d) $0.2 < x_s < 0.3$, e) $0.1 < x_s < 0.2$ and f) $0.0 < x_s < 0.1$. Figures b) through f) are shown with a Gaussian function fitted to the data.

two strips has an x_s value of 0.5. In Fig. 7, the single-layer residual distributions are shown for P0 for all x_s and for five different x_s intervals. In Table 2, the single-layer spatial resolutions for both P0 and P0′ are presented for the five x_s intervals. For P0′, which had narrower strips, the single-layer resolution varies little with x_s, but for P0 the single-layer resolution shows a strong variation with x_s. This is because the accuracy of the cluster position measurement depends strongly on the magnitude of the second highest strip charge in the cluster, which becomes very small for the wider strips as x_s approaches zero (see Fig. 4).

	Single-layer spatial resolution [μm]	
x_s	P0	P0′
0.0 - 0.1	468 ± 6	66
0.1 - 0.2	305 ± 5	64
0.2 - 0.3	161 ± 2	61
0.3 - 0.4	106 ± 1	56
0.4 - 0.5	78 ± 1	54

Table 2: Single-layer spatial resolution of P0 and P0′ for five different x_s intervals. For P0′ the statistical errors on the resolutions for P0′ for all five x_s intervals are less than 1 μm.

Figure 8 shows for P0′ the probability that a measured cluster x position lies outside a certain number of standard deviations (n) from the fitted track position. The curve was generated from the overall layer 3 residual distribution which includes clusters in all x_s ranges. For P0′ the core of this distribution is very much Gaussian with a sigma of 60 μm. The curve in Fig. 8 gives a quantitative description of its non-Gaussian tails. For example, the probability for a cluster to deviate from a predicted position by more than $3\sigma \approx 200$ μm is about 5%. Figure 9 displays the dependence of the P0′ single-layer resolution on the chamber gain for tracks with $\theta = 15°$. There is a steep dependence of the resolution on the gain up to an average cluster charge of 100 fC. Figure 10 shows the dependence of the resolution on the other track inclination angle ϕ. This angle was determined for each run from the mean of a Gaussian fitted to the track slope distribution. The resolution worsens as ϕ increases because fluctuations in the ionization density along the track distort the cluster shape more as the x-projection of the track lengthens. The measured spatial resolution is not strongly correlated with the χ^2 of the cluster fit. Figure 11 gives the single-layer spatial resolution for eight ranges of cluster-fit χ^2 normalized for each layer by the resolution for all χ^2. All six layers are included. Clusters more than 10σ from the track are excluded. The first four points represent 93% of the clusters, while 3% are in the last point, which also includes clusters with $\chi^2 > 25$. One sees that for all reasonable fits the resolution only varies by about 15%.

Figure 12 gives the spatial resolution for layer 3 as a function of the magnetic field parallel to the beam for the P0 prototype, for five ranges of x_s. The resolutions are poor because for all magnetic field values the high voltage was set below nominal, at 3.8 kV, which corresponds to a Landau peak of 45 fC. The five sets of resolutions were simultaneously fitted to the function $\sigma(\mathrm{B}) = \sqrt{\sigma(0)^2 + \kappa^2 \cdot \mathrm{B}^2}$, where $\sigma(0)$ is the resolution at $\mathrm{B} = 0$ and κ is a universal contribution characterizing the B-field effect. The simultaneous fit yielded the value $\kappa = 180$ μm/T; curves using this value for each x_s range are also plotted in Fig. 12.

The effects of including double-clusters and single-clusters with one overflow strip were investigated for both chamber prototypes. For P0′, these cluster types together make up about 7% of all clusters, and leaving them out of the analysis improves the resolutions by only about 1 μm. For P0, double-clusters and single-clusters with overflows comprise about 4% and 10% of all clusters, respectively. Excluding double-clusters from the analysis improves the resolutions by less than 1 μm. Excluding single-overflow clusters improves the resolution for the interval $0.1 < x_s < 0.2$ by 10%, and for the other x_s intervals by less than 2%.

5.3 Simulation and Six-Layer Spatial Resolution

To compare our measured single-layer spatial resolution with expectations for the CSCs and to determine the overall six-layer spatial resolution, we used a simple Monte Carlo simulation which incorporated mainly geometric and electronics effects. The simulation generated straight tracks perpendicular to the chamber, with a flat distribution in x. It assigned to each layer a cluster charge taken randomly from a distribution closely matching the measured cluster charge distribution for that layer at nominal high voltage. In each layer, the charge was placed exactly at the point where the track crossed the wire plane, and the induced charge on the five nearest strips was calculated according to the integrated Gatti function and adjusted for crosstalk. Noise was added to each strip, with a Gaussian distribution with an RMS equal to the average pedestal RMS (0.6 fC), and the strip charges were converted to ADC counts using the gain, range, and resolution of the electronics. The simulated strip data was then analyzed

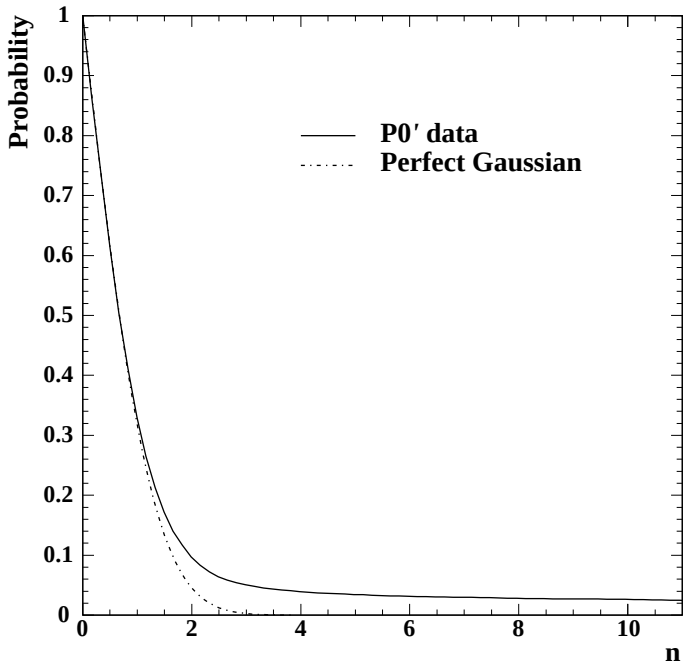

Figure 8: Probability that a measured cluster x position lies within a certain number of standard deviations of the fitted track position, for layer 3 of P0′ with the Landau peak at 100 fC. A perfect Gaussian distribution is also shown for comparison.

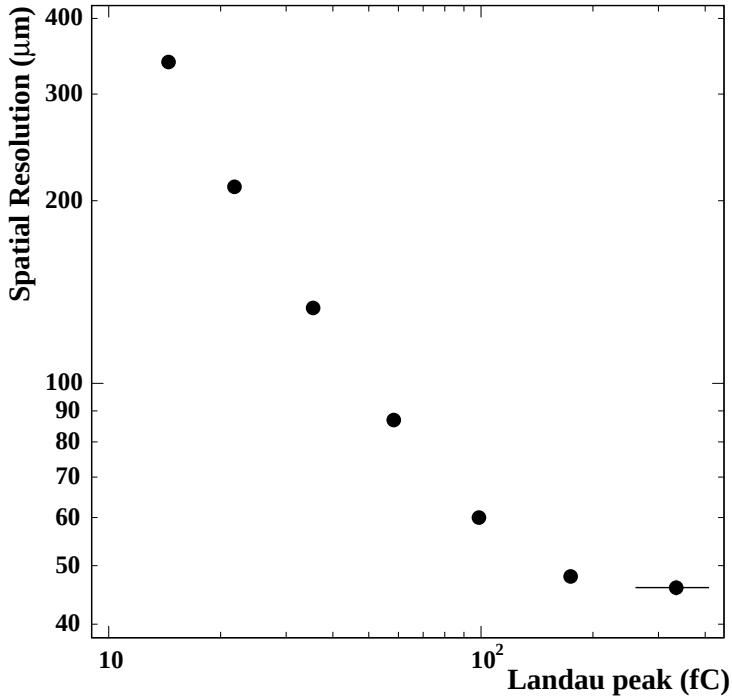

Figure 9: Single-layer spatial resolution as a function of the Landau peak position for layer 3 of P0′.

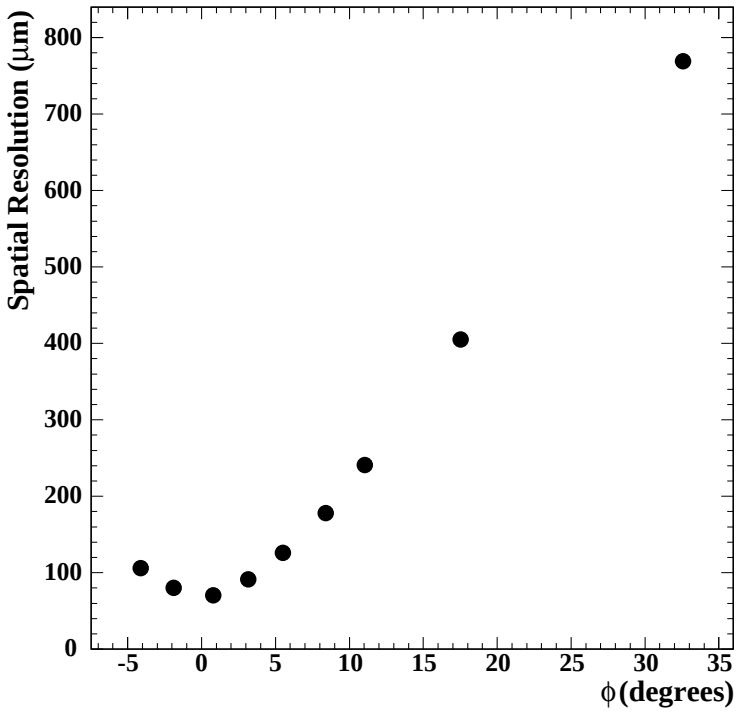

Figure 10: Single-layer spatial resolution as a function of the track incident angle (ϕ) for layer 3 of P0′.

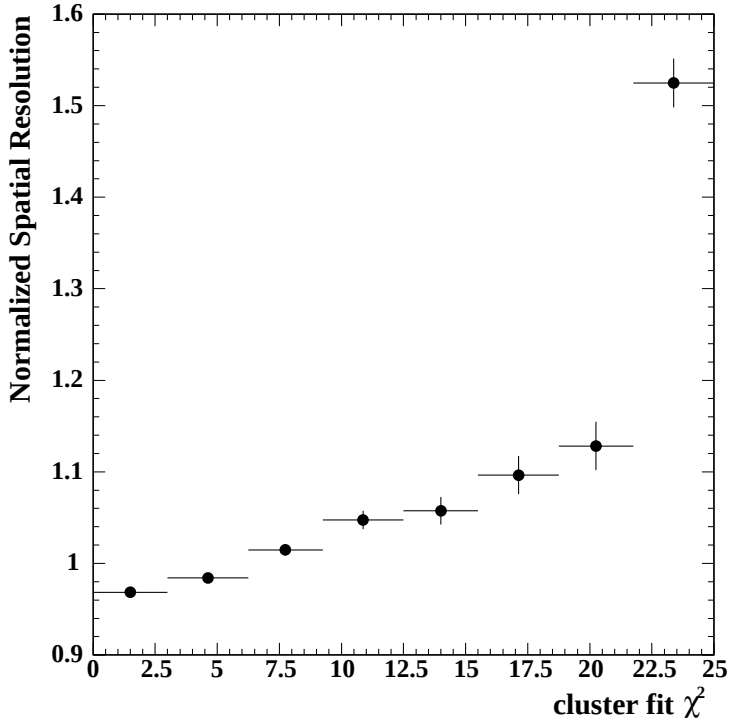

Figure 11: P0′ single-layer spatial resolution for eight ranges of cluster-fit χ^2, normalized for each layer by the resolution for all χ^2. All six layers are included. Clusters more than 10σ from the track are excluded.

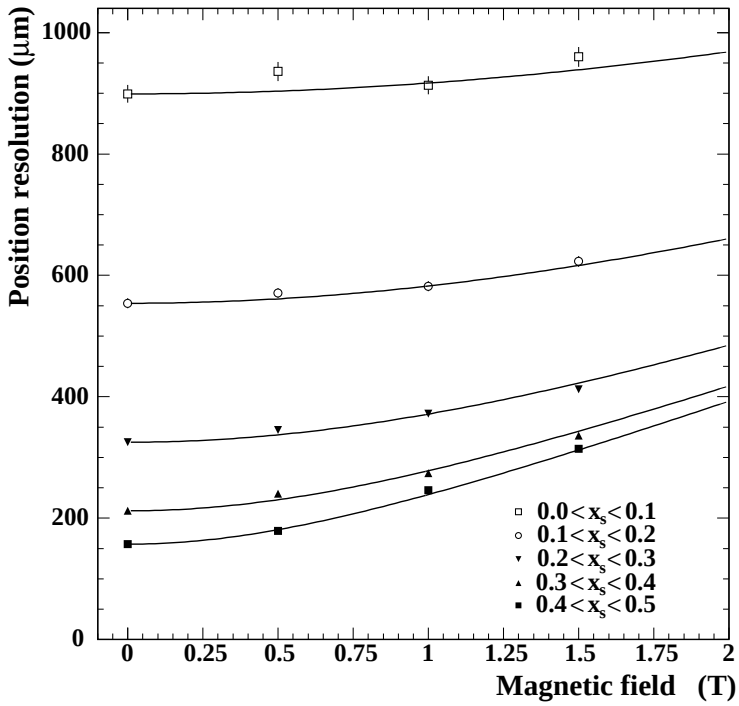

Figure 12: Single-layer spatial resolution as a function of magnetic field for layer 3 of P0, for five ranges of x_s. The curves shown are from a fit described in the text.

with a simplified version of the analysis of the real data. (No calibration or parameter-tuning errors were included, and no cuts were made against edge-effects or multi-track events.) Examples of the resulting single-layer residual distributions are shown along with data in Figs. 13a-d; the single-layer resolution of the simulation is about 15% better than the real resolution.

Before finding the six-layer resolution, we tuned the simulation to match the data even better by artificially adding uncorrelated random errors to the cluster position measurements. The added errors have a Gaussian distribution with an RMS of 40 μm for P0 and 25 μm for P0′. We also added extra hits to 1.5% of the clusters with a 4 mm Gaussian distribution with respect to the track position. The single-layer residual distributions from this tuned simulation are also plotted in Figs. 13a-d and agree much better with the data. The six-layer spatial resolution is defined as the standard deviation of a Gaussian fitted to the Monte Carlo distribution of the difference between the true (generated) track positions, at the center of the chamber, and the fitted track positions. This is shown in Figs. 13e and 13f for P0 an P0′, for both the tuned and un-tuned simulation. The fit used all layers which had good clusters as defined above (not necessarily six). The resulting six-layer resolution was measured to be 44 μm for P0, and 23 μm for P0′. These resolutions are much better than the required ones. This is desired since it leaves necessary room for additional effects, such as global chamber misalignment, worse signal to noise ratio, magnetic fields, inclined tracks and non-perpendicularity of the trapezoidal strips to the wires, which will be present in the CMS end-cap muon system and can deteriorate the chamber resolution.

The simulated single-layer residual distributions for the five x_s intervals were also compared with the data and agreed well. Although the single-layer resolution for P0 depends strongly on x_s, because of its wide strips, the variation of the six-layer resolution with x_s is much smaller and twice as fast because of the half-strip offset of the layers. The six-layer resolution ranged from 36 to 52 μm for P0, and from 22 to 23 μm for P0′.

5.4 Track Finding and Double-Cluster Recognition

The high background rates expected at the LHC require that the CMS CSCs be able to resolve events with more than one track. Therefore, we have developed a multiple-track finding algorithm which allows 4 to 6 clusters per track. Clusters are grouped into tracks in the following way. For each pair of clusters comprising one in the first layer of the chamber and the other in the last layer, a straight line is drawn between them and all clusters on intermediate layers which fall within a few millimeters of this line are selected. This procedure is repeated for all

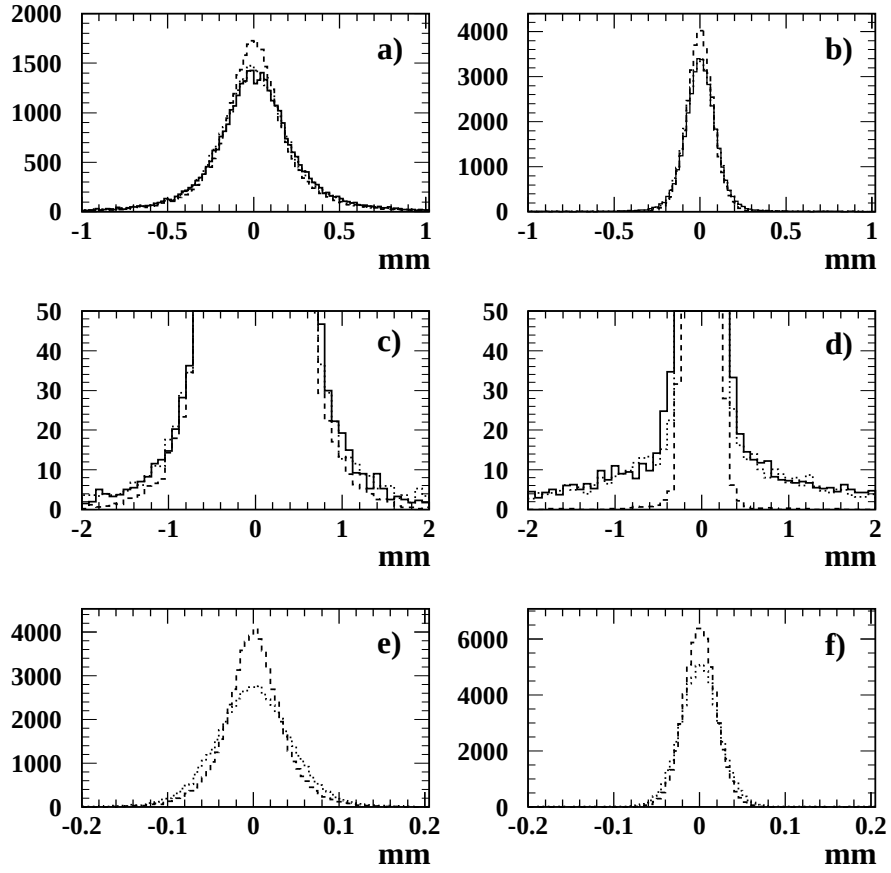

Figure 13: Single-layer residual distributions for layer 1 of a) P0, and b) P0′. The same plots are shown with an expanded scale in c) for P0, and d) for P0′. The six-layer residual distributions are presented in e) for P0, and f) for P0′. In all plots, the solid line is data, the dashed line is the untuned simulation, and the dotted line is the tuned simulation.

possible combinations of two chamber layers which could comprise the first and last layers of a track. For example, layers 2 and 5 could be the first and last layers of a 4-layer track. Clusters which can be associated with more than one track are dropped altogether. After all of the tracks for an event have been identified, residuals for each cluster in a track are calculated by excluding that cluster from the track fit and proceeding as for single-track events, with cuts made only on the other clusters in the track.

The algorithm was tested for P0′ at nominal run conditions. 41% of the multiple-track candidate events were found to have no tracks, 50% had one track, and 9% had two or more. Thus, we were able to recover about 60% of the previously rejected multiple-track candidate events. The overall layer 3 resolution (all x_s) for these events was 75 ± 3 μm, compared to the value of 60 μm found for the single-track events.

For optimization of this algorithm, it is important to know the efficiency of resolving double clusters in a chamber layer. To produce a data sample of double clusters, we overlaid two muon-induced single clusters from data taken with P0′. The position of each single-cluster was determined by the fitting method described in Section 5.2. To minimize possible bias in the double-cluster analysis, we did not apply a χ^2 cut after the fit and did not tune the h constants. In any chamber layer, it is probable that the shape of a single cluster will be distorted by δ-ray emission resulting in an imprecise determination of the cluster position. To reduce the fraction of such events, we required that the residuals (calculated from the particle positions in the other five layers) for selected single-clusters were within the range of $\pm 3\sigma$.

The resulting overlaid clusters were analyzed using an algorithm developed in [7]. In summary, it compares double-cluster and single-cluster hypotheses for the certain range of strips selected from all strips in the chamber layer. Selection of the strip range provides a smooth transition from the trivial case of well separated clusters to the case of overlapped clusters.

To select the strip range the algorithm finds the strip with maximum charge in a chamber layer (strip charge greater than 15 fC[3)] and no ADC overflow). This strip and ± 2 adjacent strips make the first region of interest (ROI). Then, excluding the strips contained in the first ROI, it finds the strip with the next highest charge (again the strip charge must be greater than 15 fC). This strip and ± 2 adjacent strips make the second ROI. The algorithm then selects the range of strips containing all ROIs that were found (one or two) and adds one more strip at the beginning and end of the range. In the most interesting case of single clusters close to each other (separated by not more than two strips) the algorithm selects a 7-strip-wide range around the strip with the maximum charge.

In an experiment such as CMS, we will not know before hand if we are looking at double clusters or, just wide single clusters, so it is interesting to know how well we can distinguish the two cases. To study this, we fitted the selected range of strips first assuming they comprised a double cluster and again assuming they comprised a single cluster. The double-cluster fit used two overlapping integrated Gatti functions and had three parameters: the position and amplitude for the first cluster, and the position of the second cluster. (The amplitude of the second cluster was fixed by normalization.) The single-cluster fit, similar to the one described in Section 5.2, had just one parameter: the cluster position. The group of strips was identified as a double cluster if its shape was better fitted by the double-cluster than the single-cluster hypothesis.

In Fig. 14 we show the efficiency for identifying double clusters as a function of the distance between the two clusters. Note that our analysis will produce a slightly lower estimate of the efficiency because of a $\sqrt{2}$ noise increase due to the overlaying of events. One sees that a 90% efficiency for distinguishing double-clusters is reached when the clusters are separated by at least one-half the strip pitch (3.175 mm).

6 Timing Resolution from the Anode Wires

In the CMS end-cap muon system, anode wire times will be used at the trigger level to associate the muon track with the correct beam crossing. Anode hit positions will also provide a crude position measurement in the direction parallel to the strips.

6.1 Low Electric Field Regions

A simple single-layer CSC will not produce a good timing resolution because of the existence of very low electric field regions between the anode wires. We therefore expect to see late timing information for tracks which leave

[3)] To reduce the bias in our analysis caused by a higher noise in overlaid events we use a somewhat higher charge threshold than in Section 5.2.

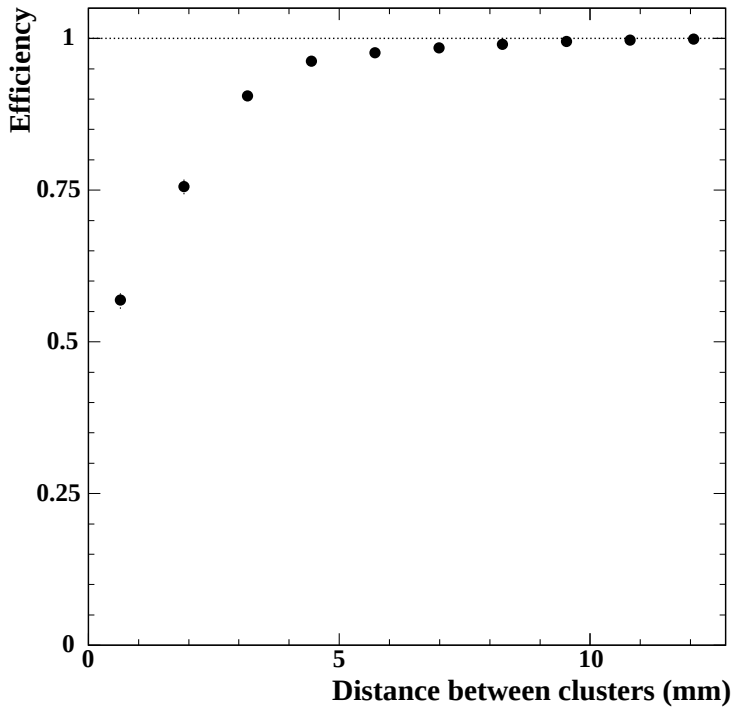

Figure 14: Efficiency for reconstructing two clusters in P0′ as a function of the distance between them.

a significant portion of their ionization in the area around this region. We have used the information from the external SiBT to verify this effect in detail. Figure 15 shows a scatter-plot of the time measured by a single wire group versus the track position perpendicular to the wires, as extrapolated from the SiBT. The data were taken from a single wire group of 9 wires with threshold discriminators. (Note that on this and subsequent figures, small numbers correspond to late times because of the common stop discriminators used in the experiment.) One can see in this plot the positions of the 9 anode wires in the group. In addition to late time measurements caused by noise and ionization statistics, the late times from the low field regions between the wires appear as fingers of points extending downward. Late times are associated with tracks located at the midpoint between wires.

Late anode wire times are also visible as a tail in the single-layer anode wire time distribution shown in Fig. 16a. These data were taken with the beam normal to the anode wire plane. The presence of late anode wire times can be avoided by rotating the chamber with respect to the incoming muon, since, for every track, some of the ionization will be deposited outside of the low-field region. In Fig. 16b the single-layer anode wire time distribution is shown for data taken with the chamber rotated to an angle $\theta = 15^\circ$ with respect to the muon beam, along with the result of a Gaussian distribution fitted to the data. The width of this distribution is 8.8 ns. The situation is even more improved when one uses multi-layer CSCs, since a typical inclined track is expected to pass close to the anode wires in at least some of the layers.

6.2 Anode Wire Track Finding Procedure

Because in the actual CMS detector the end-cap muon chambers will be extremely large and the backgrounds are expected to be severe, only certain patterns of anode wire hits on the six layers should be considered in determining if a track is present and what its associated time is. In forming these patterns, only hits which fall inside a particular broad time window should be used.

For this analysis we have implemented in software a procedure that models what will be implemented in the CMS muon trigger hardware. For each angle θ at which data were taken, we defined a table of patterns which gave the offsets of the anode hits in the various layers with respect to a single reference layer. A diagram showing typical wire hit patterns for particle trajectories at normal incidence and at $\theta = 40^\circ$ is shown in Fig. 17. Patterns like these are “slid” along the length of the chamber looking for a match. This occurs when there are in-time hits on all six layers for the present location of the pattern. “In-time” here means falling within a broad time window with a width of 200 ns. This window was chosen to exclude spurious time hits not associated with the passing muon.

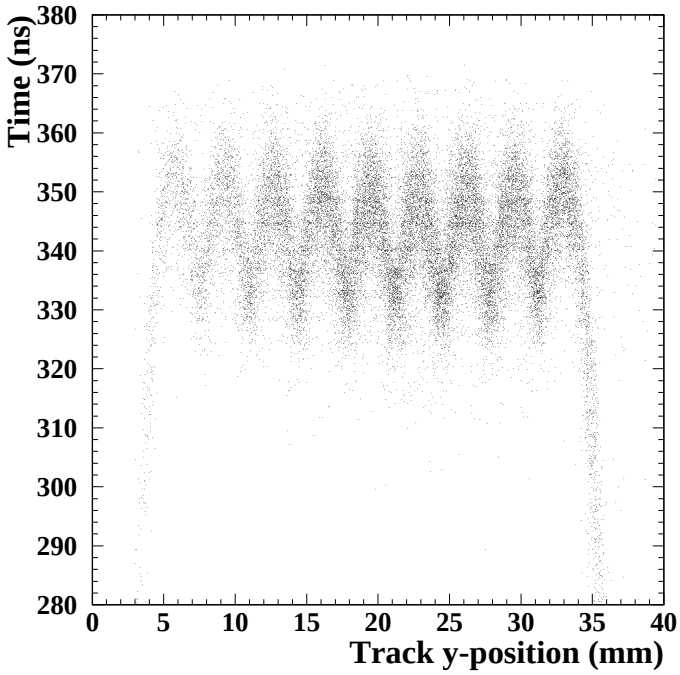

Figure 15: The measured time from a single wire group vs. the position of the track perpendicular to the wire direction, as inferred from the SiBT. The data were taken from a single wire group of 9 wires with threshold discriminators. Early times correspond to the top of the figure.

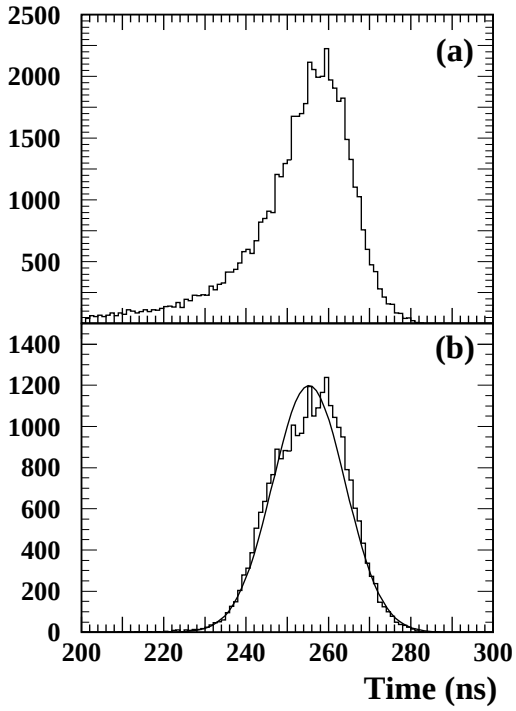

Figure 16: Single-layer anode wire time distribution for layer 1 of P0′ for a) data taken with the beam at normal incidence and b) at an angle $\theta = 15^{\circ}$. A Gaussian fit to the data is shown in b).

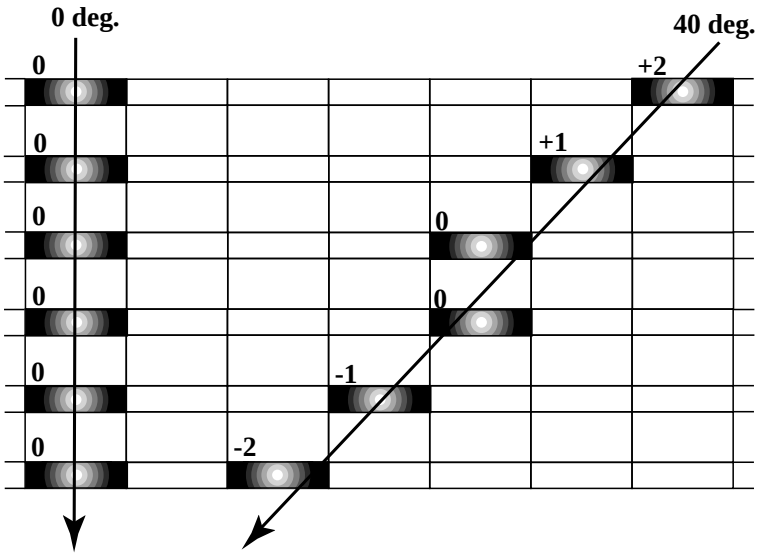

Figure 17: Typical hit wire patterns representing tracks in the anode wires for data taken with the beam at normal incidence and at $\theta = 40^\circ$. Tracks were found by matching the hit anode wire groups in each layer to patterns representing valid track trajectories. The numbers in the figure are the anode hit offsets with respect to the anode hit in layer 3.

If no match was found for the first pattern, then the next pattern is used and so on. After looking for matches with hits on all six layers, we reduce the requirement to only five out of six, and then to only four out of six. Anytime a match is found, the associated hits were removed from further consideration. Thus, we were able to identify multiple tracks if they were sufficiently separated. The tables of patterns are angular dependent and were ordered so that the most common patterns were tried first. We find that 99% of the events in which we found a matching pattern could be matched with one of the six most common patterns.

One additional cut was applied to the data. Any event where the pattern extended off the edge of the chamber was removed. For most experimental conditions this cut removed no events. Only when the chamber was rotated to angles $\theta \geq 25^\circ$ did this cut remove a number of events which was significant compared to the inefficiencies quoted. In this case, the cut removed events where the track clipped the edge of the chamber. We believe that this cut does not bias our answers unfairly in these cases. We did not remove the small fraction of events (typically a few percent) in which the presence of unused hits suggested that a second track was present but not found by the pattern matching procedure. Removing these events produced a small increase in our measured efficiencies, presumably because these events contained overlapping tracks which were not correctly matched.

6.3 Six-Layer Timing Results

There are several options for combining independent time measurements from multi-layer CSCs to produce the best estimate of the time a muon passed through the chamber. For our purposes, we consider a timing estimator to be "good" to the extent that it would associate a muon track with the proper LHC beam crossing. Hence, the probability that the time from the estimator falls within a 20 ns window is taken as a measure of efficiency. We use 20 ns instead of the LHC beam crossing time of 25 ns to try to account for timing offsets in the trigger electronics. The center of the 20 ns window is adjusted to maximize the efficiency for each case. Calculations show that a system of four stations, each consisting of a six-plane CSC which is capable of tagging the correct bunch crossing with 92% efficiency, will be capable of assigning detected muon tracks to the correct bunch crossing with greater than 99% efficiency.

The analysis consisted of two steps: 1) apply the pattern matching procedure; 2) calculate a time for the track based on certain estimators (we consider several here). For each step we define an efficiency. The first of these will be referred to as the tracking efficiency, and the second as the timing efficiency. The overall efficiency is the product of the two.

The time estimators we use involve first time-ordering the anode hits from a found track. Then we take either the earliest time, the second earliest, etc., up to the fourth earliest as our four possible time estimators. Shown

in Fig. 18 are the corresponding timing efficiencies as a function of the Landau peak position from the cathode strips for both of the discrimination schemes. Curves for the four different time estimators are also given. The best timing efficiency is typically obtained with the second earliest time for threshold discriminators and the third earliest for zero-crossing. In any case the difference between the timing efficiency resulting from the second and the third earliest times is small, so we have chosen to use the second earliest time.

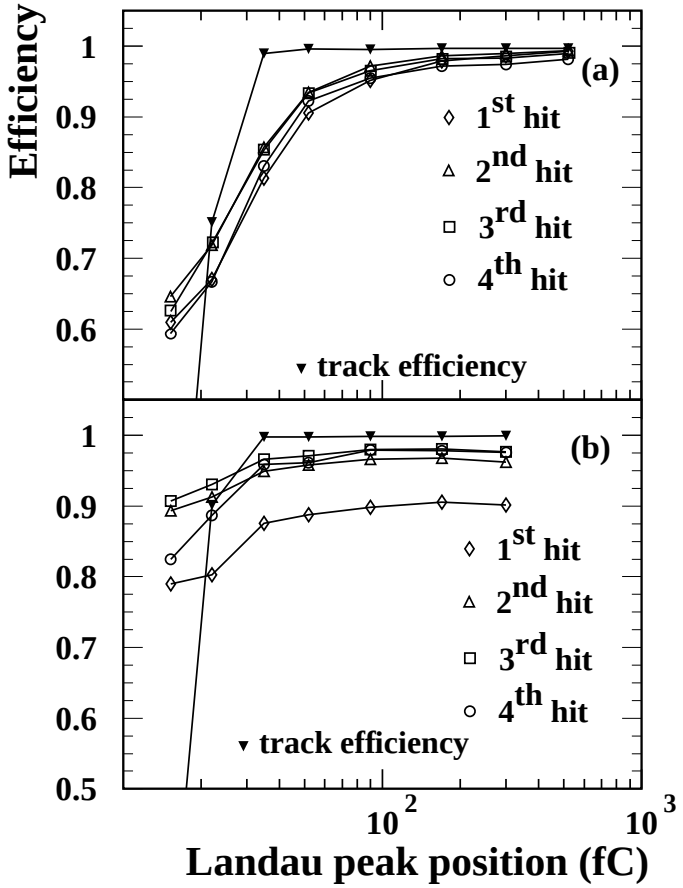

Figure 18: The timing efficiency of P0′ with respect to an optimum 20 ns window as a function of the Landau peak position from the cathode strips for a) threshold discriminators and b) zero-crossing discriminators. The four curves in each figure correspond to using the first, second, third, and fourth earliest times as estimators. Also plotted here is the track efficiency due to the pattern finding procedure.

The tracking efficiency is also plotted in Fig. 18. As expected, this dominates the overall efficiency at low gains. At high gains, the tracking inefficiency drops to typically a few times 10^{-3}. We believe that this represents noise triggers, but in any case it is very small compared to the remaining timing inefficiency. In all subsequent plots, we use the timing efficiency resulting from the second earliest anode hit from the found track.

In Fig. 19a the efficiency as a function of the Landau peak position is given, this time comparing threshold and zero-crossing discriminators as well as the effect of the change in wire spacing between P0 and P0′. The insensitivity of the timing resolution to operating voltage for the zero-crossing scheme is seen in this figure, although this comes at the cost of a slightly lower efficiency at the highest gains. This robustness against changes in the gain of the chamber is further demonstrated in Fig. 19b which shows the location in time of the center of the 20 ns window used to measure the efficiency. Again, larger numbers correspond to earlier times. Our requirement of 92% efficiency is met in all cases when the strip cluster charge is above about 60 fC. A 95% efficiency is reached for our nominal high voltage setting with a Landau peak of 100 fC.

The clean environment at the H2 test beam and the small sizes of the chambers tested made it possible to perform a simpler timing analysis by taking the earliest time of all hits on a given layer as the "layer time" and not requiring that the hits form a pattern. Such an analysis has been performed, and yielded results which were identical to those obtained with the pattern matching analysis. This rules out the possibility that the pattern matching analysis underestimates the efficiency due to pattern finding problems. The pattern finding analysis, in turn, rules out the

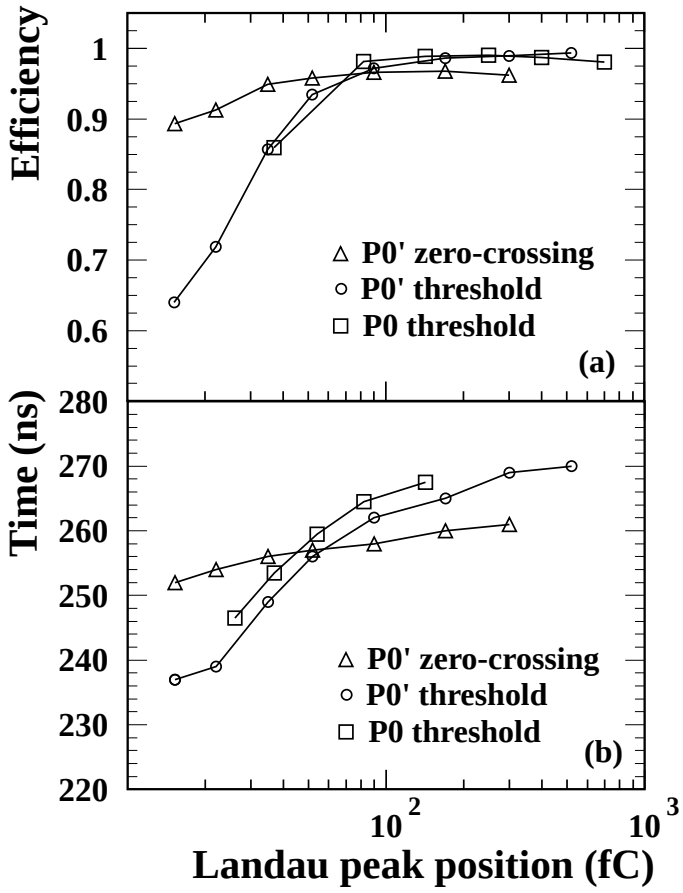

Figure 19: a) Timing efficiency and b) the center of the 20 ns window used to optimize the efficiencies, both as a function of the cathode strip Landau peak position. Data are shown for P0′ with threshold discriminators and zero-crossing discriminators, and for P0 with threshold discriminators. Data were taken with the beam at $\theta = 15^\circ$ (P0′) and between 5° and 30° (P0).

possibility that the other analysis overestimates the efficiencies due to hits beyond those legitimately associated with a single beam muon.

6.4 Variations in Angle and Magnetic Field

The effect of changes in the angle θ between the beam and the normal to the plane of the chamber is shown in Fig. 20. As the chamber was rotated, the ionization from the track was collected on multiple wires. An essentially flat efficiency was measured over the angular range relevant for the CMS end-cap muon system (10° to 44°). A dip in the efficiency for the threshold discriminators occurs at normal incidence due to tracks which pass through the low-field region mid-way between wires. This effect is reduced in the data taken with zero-crossing discriminators due to their greater dependence on the bulk of the ionization.

The timing efficiency as a function of the magnetic field normal to the chamber is shown in Fig. 21 for the P0 prototype for two different chamber high voltages. A small degradation in the timing resolution is observed for the data taken at low gas gain and large values of the magnetic field. We also show two additional data points at higher gas gain. (No further data points were available at this gain.)

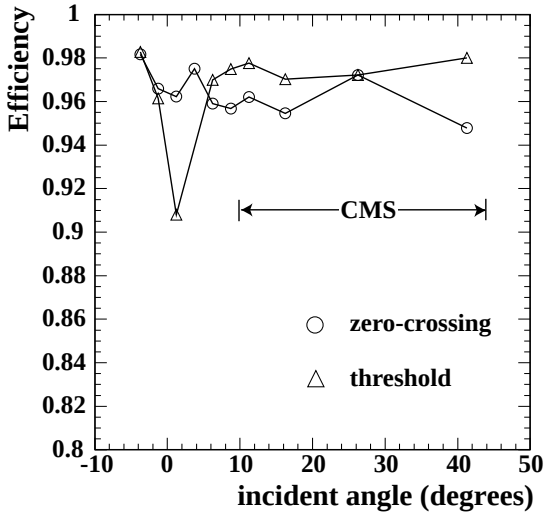

Figure 20: Timing efficiency for P0′ as a function of the incident angle θ for both zero-crossing and threshold discriminators. The relevant angular range for incident tracks in the CMS end-cap muon system is indicated on the figure.

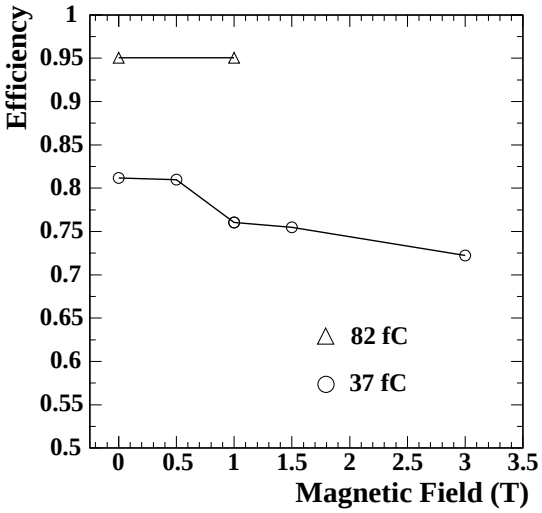

Figure 21: Timing efficiencies as a function of the magnetic field applied normal to the plane of the P0 chamber. The beam was also normal to the chamber and threshold discriminators were used. Data are shown for two different gains: the cathode strip Landau peak at 82 fC (triangles) and 37 fC (circles).

7 Conclusions

We have performed tests using a high momentum muon beam on two CSC prototypes which were built to resemble two different sections of the CMS end-cap muon detector CSCs. Both prototypes were tested with various values of high voltage and incident track angles. The P0 prototype was also tested in a magnetic field. For the P0 chamber (15.88 mm strip pitch) the single-layer spatial resolution ranged from 78 μm to 468 μm and for P0′ (6.35 mm strip pitch) from 54 μm to 66 μm. The variation in the single-layer spatial resolution depends on whether the incident particle passed between two cathode strips or through the center of a strip. The six-layer spatial resolution was estimated by using a Monte Carlo program tuned to reproduce the data. For P0 the six-layer resolution was found to be 44 μm, for P0′ 23 μm. The efficiency for collecting an anode wire signal from one of the six layers within a 20 ns time window was found to be greater than 95% for a gas gain providing an average collected charge of at least 100 fC on the cathode strips.

Acknowledgements

The authors are grateful to O. Alford for his contributions to the design of the chamber and to F. Chase for his efforts in its construction. The authors would like to thank G. Bencze for his valuable help at the H2 beam line and F. Szoncso for the H2 data acquisition system. We acknowledge the excellent work of P. Petiot and G. Waurick who constructed the chamber supports and the rotating table on which we mounted the chamber while in the beam line. We are also grateful to the group from the Helsinki Institute of Physics for providing the Silicon Beam Telescope.

This work was performed under the auspices of the U.S. Department of Energy under contract numbers W-7405-Eng-48, DOE-ER-40682-115, DE-FG02-92ER40697, DE-FG03-91ER40662 and DE-FG03-94ER40837, and the US National Science Foundation under grant number 95-14950.

References

[1] The CMS Technical Proposal, CMS Collaboration, **CERN/LHCC 94-38** (1994).

[2] G. Charpak et al., Nucl. Instr. and Meth. **167** (1979) 455.

[3] E. Gatti et al., Nucl. Instr. and Meth. **163** (1979) 83.

[4] J.C. Santiard et al., *GASPLEX A Low Noise Analog Signal Processor for Readout of Gaseous Detectors*, **CERN-ECP/94-17**.

[5] I. Hietanen et al., Nucl. Instr. and Meth. **A 310** (1991) 671, 667.

[6] E. Mathieson and J.S. Gordon, Nucl. Instr. and Meth. **227** (1984) 277.

[7] V. Gratchev et al., Nucl. Instr. and Meth. **A 365** (1995) 576.